RSC Advances

PAPER

View Article Online
View Journal | View Issue

Cite this: *RSC Adv.*, 2020, **10**, 16817

Nanostructured manganese oxides electrode with ultra-long lifetime for electrochemical capacitors

Madhu Gaire, *[a] Kun Liang,[a] Sijun Luo,[a] Binod Subedi,[a] Shiva Adireddy,[a] Kurt Schroder,[b] Stan Farnsworth[b] and Douglas B. Chrisey *[a]

Received 4th February 2020
Accepted 29th March 2020

DOI: 10.1039/d0ra01081b

rsc.li/rsc-advances

We describe the instantaneous fabrication of a highly porous three-dimensional (3D) nanostructured manganese oxides-reduced graphitic oxide (MnO_x-rGO) electrode by using a pulse-photonic processing technique. Such nanostructures facilitate the movement of ions/electrons and offer an extremely high surface area for the electrode/electrolyte interaction. The electrochemical performance was investigated by cyclic voltammetry (CV), galvanostatic charge–discharge (GCD) and electrochemical impedance spectroscopy (EIS) with 1 M KOH as the electrolyte. The as-prepared thin film electrode exhibits excellent electrochemical performance and an ultra-long lifetime by retaining 90% of the initial capacitance even after 100 000 GCD cycles at constant areal current density of 0.4 mA cm^{-2}. We attribute this excellent lifetime performance to the conductive reduced graphitic oxide, synergistic effects of carbon composite and the metal oxides, and the unique porous nanostructure. Such highly porous morphology also enhances the structural stability of the electrode by buffering the volume changes during the redox processes.

1. Introduction

Electrochemical capacitors possess a high-power density, superior cycling stability, and excellent charge/discharge characteristics, making them one of the most promising candidates for applications ranging from electronics to hybrid electric vehicles.[1,2] They can be further classified into electrochemical double-layer capacitors (EDLCs), in which the energy storage is achieved through charge separation at the electrode/electrolyte interface, and pseudocapacitors, in which the energy storage is achieved through faradaic redox reactions.[3] Generally, the EDLCs use carbon-based materials and the pseudocapacitors use metal oxides and conductive polymers as electrodes. For high gravimetric energy storage, metal oxides based on pseudocapacitors have attracted special attention because of their higher energy density than EDLCs due to the fast and reversible redox reactions taking place on or near the surface of the electrode material along with its fast charge/discharge processes.[4,5]

Past work has studied several transition metal oxides, such as RuO_2, Co_3O_4, NiO, Fe_2O_3, MnO_2, *etc.*[6,7] Among them, RuO_2 has been the most extensively studied material due to its high theoretical capacitance, high conductivity, and long cycle life. However, its practical application has been limited by low abundance, higher cost, and toxicity.[8,9] Therefore, research has been devoted to finding alternative materials that are inexpensive, abundant, and have capacitive performance comparable to RuO_2.[10] In this regard, manganese oxide (MnO_2) has been considered as an excellent candidate because of its low cost, high theoretical capacitance and environmental compatibility.[11]

The most important parameters that could affect the electrochemical performance of the electrode are its nanostructure, morphology, and electrolyte. This is why the fabrication of MnO_2 electrode with highly porous nanostructure is of crucial importance for achieving high capacitance[12] because such structures offer a high surface area and help improve the electrochemical performance. As far as electrolytes are concerned, organic electrolytes have a wider working potential window compared to aqueous electrolytes, but their drawbacks, such as high viscosity, poor ionic transportation, lower electronic conductivity, and toxicity limit the electrode's performance.[13,14] On the other hand, aqueous electrolytes are inexpensive, safe, easy to handle and have high conductivity. Therefore, in this work, we have used 1 M KOH as the electrolyte because of its high OH^- ions mobility.[15]

In the recent past, different methods, including seeded low-temperature hydrothermal growth,[16] chemical vapor deposition,[17] and chemical reduction[18] have been reported for the fabrication of high-performance nanostructured manganese oxide electrodes. However, the drawbacks such as poor conductivity and volume change resulting from redox reactions during the charge–discharge process limit their practical application. It is especially the volume change during redox reactions that leads to the electrode's poor structural stability, which eventually results

[a]*Department of Physics and Engineering Physics, Tulane University, New Orleans, Louisiana, 70118, USA*
[b]*NovaCentrix, Austin, Texas, 78728, USA*

in poor cycle life. For their application in long-term electronic devices, the electrodes' lifetime needs to be enhanced. One of the ways to improve the lifetime is to add conductive carbon materials to form a metal oxide and carbon composite electrode. In this regard, the fabrication of transition metal oxide/carbon composites electrodes for supercapacitors have been reported[19–29] using various methods. However, no industrial technology for the fabrication of composites has been reported yet. Recently, our group reported a unconventional, low-cost and high-throughput pulsed photoinitiated approach to the *in situ* formation of three-dimensional (3D) nanostructured composited thin film composed of nanocrystalline transition metal oxide and reduced graphitic oxide through flash xenon lamp irradiation of metal–organic precursor films.[30–32]

Herein, we report a one-step thin-film processing method and excellent cyclic stability and ultra-long cycle life of the electrode. Firstly, we have followed a spray-coating technique, which can be accomplished in less than a minute in ambient conditions, to spray Mn-acetylacetonate precursor solution onto the Pt-coated Si substrate. To process the as-sprayed thin film, we have used a novel pulse-photonic curing technique to prepare a manganese oxide-reduced graphitic oxide (MnO_x-rGO) nanocomposite thin film electrode. By following this highly scalable technique, we processed the thin film electrodes in several seconds, which is a significant reduction in processing time in comparison to the conventional techniques which would take from minutes to hours for processing. The as-prepared electrode has a highly porous 3D surface and contains dendritic structure, which increases ion/electron diffusion as well as provides a large specific surface area for the electrode/electrolyte reactions. The as-prepared MnO_x-rGO composite shows pseudocapacitive behavior with the presence of redox peaks in the cyclic voltammetry (CV) curves and exhibited a specific capacitance of 11 mF cm^{-2} at constant areal current density of 0.4 mA cm^{-2}. Secondly, we want to report the excellent electrochemical performance of the as-prepared electrode. Due to the combined effect of optimum processing conditions, desirable highly porous nanostructures, and the directly grown nanostructure on the substrate, which eliminates the need for a binder, as prepared electrode shows ultra-long lifetime by retaining 90% of the initial areal specific capacitance even after 100 000 continuous charge–discharge cycles at a constant areal current density of 0.4 mA cm^{-2}. Such long cyclic stability makes the as-prepared electrode a potential material for application in long term energy storage devices. These excellent results can be attributed to the increased conductivity of the binder-free electrode and highly porous morphology, which buffer the volume changes. Furthermore, such morphology helps enhance the structural stability of the electrode and allows for a large portion of the active material to take part in redox processes, resulting in high capacitance, and ultra-long cycle life.

2. Experimental section

2.1. Thin film deposition

Organometallic precursor Mn(III)-acetylacetonate powder (Sigma Aldrich) was dissolved in acetone (Sigma Aldrich) to prepare a saturated solution. The substrate was cleaned before spray-coating by ultrasonic treatment with acetone and deionized water. The precursor solution was then spray coated in ambient condition on Pt-coated silicon wafer (University Wafer, USA) with the help of an air spray gun (Paasche Airbrush, Chicago). After the solvent (acetone) evaporated, the precursor solution remained as a uniform precursor film on the substrate.

2.2. Synthesis of highly porous 3D nanostructured manganese oxide

The as spray-coated precursor film was processed by using a pulsed-photonic curing system (PulseForge 1300, NovaCentrix Corp., Austin, Texas) with an output spectrum between 220–1000 nm and peaked at 450 nm. The pulsed light irradiation parameters (*e.g.*, number of pulses, applied voltage, pulse length, *etc.*) were controlled with the help of a computer, and the energy density of a pulse sequence onto the samples was measured by an integrated bolometer before starting the irradiation. The photonic curing parameters used were: 600 V, envelope width: 1950 μs, μpulses: 5, fire rate: 1.2 Hz, pulse fluence: 5.6 J cm^{-2}, number of pulses: 2. The pulsed-photonic curing system uses the flashlight from a xenon lamp to process the thin films in ambient conditions. It is well-known that transition metal acetylacetonate (acac) complexes such as Co-acac, Ti-acac, Fe-acac, and Mn-acac absorb the visible light. Our previous work found that the pulsed light irradiation results in the photoinitiated chemical reaction of the metal-acac molecules for the *in situ* formation of metal oxide-reduced graphitic oxide nanocomposite thin films.[30–32] In this work, it was also found that the Mn-acac precursor absorbs the visible light during the pulsed light irradiation, resulting in the formation of a nanostructured composite thin film electrode. The first pulse irradiation produced a sharp and loud sound, possibly because all the Mn-acac molecules transformed into MnO_x-reduced graphitic oxide (rGO) after the absorption of enough light energy. The second pulse irradiation worked similarly as the traditional post-photothermal treatment of MnO_x-rGO. After the pulsed-photonic processing, the spray-coated Mn-acac precursor film was transformed into a solid nanostructured conductive thin film.

2.3. Photonic processing, nucleation, and growth

Nucleation and growth of the oxide material on the substrate determines nanostructure and as such is crucial to the electrochemical performance of the electrode. By controlling the film growth, which is a highly non-equilibrium process, we can improve the mobility of the charge, that in turn determines the performance of the electrode. The pulsed photonic processing rapidly heats the film and in a concomitant manner, it rapidly cools after the pulse. The rapid cooling will trap metastable phases and nanostructures. Initially, the film cools *via* conduction on the substrate and subsequently through the porous MnO_x-rGO nanostructure. The film growth and nanostructure formation occur during the irradiation by the 2 pulses as previously described.

The film growth is preceded by the photonic pyrolysis of the precursor. During the photothermal treatment of the as-sprayed films, as we overcome the surface-volume energy barrier, nucleation, and growth of oxide material starts. As opposed to

the conventional laser-based chemical vapor deposition (LCVD) which has a small exposure area with short pulse length and a fixed wavelength, photonic processing with the PulseForge can be done in a quick and roll-to-roll manner (in case of flexible substrates) because of its extremely short processing time, large exposure area, and broadband spectrum. Furthermore, the pulsed light in photonic curing has higher fluence, which means that higher processing temperature can be attained without damaging the substrate. At the initial stage of the nucleation, the thermal energy from the photonic processing causes atoms or molecules to condense and, undergo surface diffusion and migration to form a continuous film. Thin-film growth by conventional vapor deposition methods typically occurs *via* one of three different mechanisms: island growth, layer-by-layer growth and mixed growth.[33] For high conductivity films, it is desired to have layer-by-layer growth, which is beneficial to the performance of the electrodes, as opposed to 3D-like island growth that gives rise to voids in the film. The two most important parameters for nucleation and growth are the energy barrier to surface diffusion (Ediff) and the energy barrier to desorption (Edes).[34] The nucleation density of the films depends directly on these energy barriers. Most importantly, a smaller diffusion barrier is advantageous for the nucleation and growth as this results in higher surface mobility, which results in more chances for molecules to interact with one another and form a stable cluster. The smoothness of both the substrate and the as-sprayed metallic film is of crucial importance as the rough surface limits the electrical conductivity due to the electron scattering at grain boundaries.[35]

During the photonic curing process, we propose that the heterogeneous nucleation takes place (i) at the interface between the substrate and the precursor film, (ii) throughout the precursor film and (iii) between nanoparticles at the top of the film. The irradiation of the precursor film with the first pulse results in the formation of the bottom dense layer whereas the subsequent pulses result in the nucleation of nanoparticles and eventually the necking of the nanoparticles starts, as shown in nucleation and growth schematics Fig. 1. Further pulsed irradiation removes organic matter that hinders the sintering. Additionally, with the increasing number of pulses the temperature gets higher, which results in activation of the nanoparticles, the rapid growth of nanoparticle necking and the densification of the sintering neck. Finally, we get a conductive sintered thin film with a dendritic top layer and a dense bottom layer. Along with being nearly instantaneous, the other advantage of photonic synthesis is that as-cured metal oxide films show a higher surface roughness than thermally annealed ones due to the aforementioned rapid introduction of thermal energy that minimizes re-crystallization by not allowing self-diffusion of the metal oxide.[36] This provides more active sites for electrode–electrolyte interaction which enhances the electrochemical performance of the electrode.

2.4. Characterization methods

The surface and cross-sectional morphologies of the as-prepared MnO_x-rGO electrode were studied by using a field-emission scanning electron microscopy (SEM) (Hitachi S-4800, Hitachi Corp., Tokyo, Japan). X-ray diffraction (XRD) patterns were collected using a powder diffractometer (Rigaku Smart Lab, USA) configured with a Cu K_α radiation at 40 kV voltage and 40 mA current. Raman spectrum measurement was carried out using a DXR Raman Microscope (Thermo Scientific, Massachusetts, USA) with a 532 nm laser as the excitation source.

The electrochemical properties were studied by cyclic voltammetry (CV), galvanostatic charge–discharge cycling (GCD) and electrochemical impedance spectroscopy (EIS) in a three-electrode experimental setup using potentiostat/galvanostat (Model M204, Autolab, Metroohm, The Netherlands) with a Hg–HgO (CH Instruments, cat. no.152), platinum wire and MnO_x-rGO being reference, counter and working electrodes, respectively. The CV and GCD tests were done in the potential range of 0–0.6 V *vs.* Hg–HgO and EIS measurements were carried out with a sinusoidal signal of 10 mV over the frequency range from 1 MHz to 10 mHz. All the measurements were carried out in 1 M KOH aqueous electrolyte solution at room temperature (23 °C).

3. Results and discussion

3.1. Nanostructure characterization

The surface morphology of the as-prepared MnO_x-rGO was observed by SEM, which is shown in Fig. 2. In supercapacitors, the surface morphology of the electrode plays a significant role in its performance as the electrochemical reactions take place on (or near) the active material surface.[4,6] From surface SEM images, we can see that the as-prepared MnO_x-rGO electrode has a highly porous 3D structure, which is desirable for a supercapacitor electrode as capillary force mechanism in such morphology helps enhance the electrochemical performance due to the increased mass transport and diffusion of the electrolyte into the electrode.[37] The porous morphology contributes to improving charge storage capacity because it provides a large specific surface area for the active material and electrolyte interaction. Therefore, most of the material is accessible to the electrolyte that in turn results in lower series resistance due to open transport paths. As such, it enhances ion diffusion in the charging and discharging processes that eventually contributes to the better electrochemical performance of the electrode. Furthermore, such porous morphology is advantageous to enhance the exploitation of the active site of the electrode material through intercalation and extraction of electrolyte ions, resulting in better electrochemical behavior.[6] From the cross-sectional SEM image, it can be easily seen that the electrode has a dense bottom layer and a porous and dendritic top layer, with each dendrite of size around 50 nm. Such dendritic structures increase ion/electron diffusion, resulting in better performance.

3.2. XRD analysis

The phase and composition of the as-prepared electrode was analyzed by X-ray diffraction (XRD), which is shown in Fig. 3. It is noted that three strong peaks can be found in Fig. 3, which can be associated with Pt from the substrate. Two characteristic peaks located at 35.2° and 43.8° are well indexed with randomly

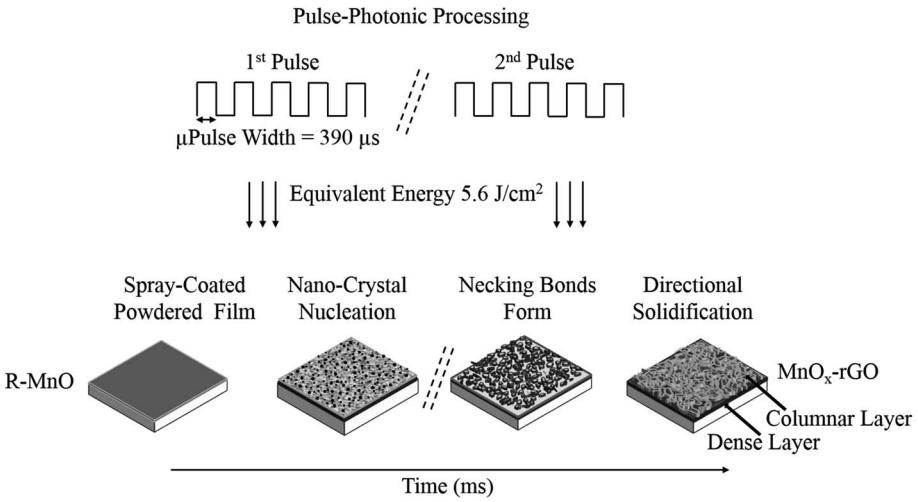

Fig. 1 Schematic illustration of nucleation and growth of the nanoparticles during photonic processing ("R" refers to the organic component in the film).

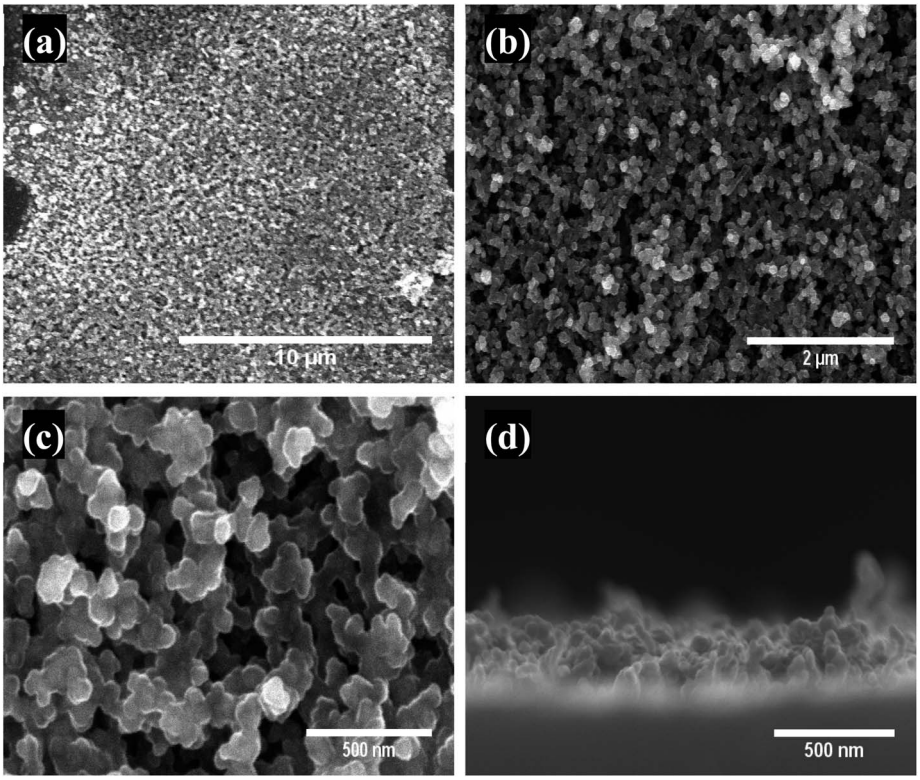

Fig. 2 (a–c) Low to high magnification SEM surface images showing porous morphology and (d) cross-sectional image showing dendritic top layer of MnO_x-rGO electrode.

oriented grains of Ramsdellite, which is an orthorhombic MnO_2.[38] Additionally, two more peaks at 59.1° and 66.1° are also observed due to randomly oriented grains of Mn_3O_4.[39] The above analysis demonstrates that the as-prepared electrode exists as a composite of MnO_2 and Mn_3O_4, which can be directly used as an electrode without any organic binders in supercapacitor.

3.3. Raman spectroscopy analysis

Raman spectroscopy is an effective and nondestructive technique to investigate the structural characteristics and the chemical composition of carbon-based materials. Fig. 4 shows the Raman spectrum of the as-prepared nanostructured MnO_x-rGO electrode. From the figure, Raman bands from 200 to

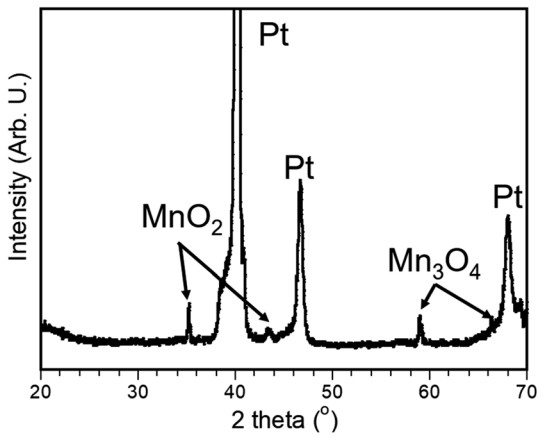

Fig. 3 XRD pattern of MnOx-rGO electrode.

1000 cm^{-1} are present due to the Mn–O vibration of manganese oxides. Three peaks centered at 311, 364 and 653 cm^{-1} are in good agreement with the literature.[40,41] The peaks at 311 cm^{-1} and 364 cm^{-1} are attributed to the out of plane bending modes of Mn–O and the asymmetric modes of bridge oxygen species (Mn–O–Mn), while a sharp peak 653 cm^{-1} corresponds to A_{1g} mode due to the Mn–O breathing vibration of divalent Mn ions in tetrahedral coordination.[41] The presence of D (1350 cm^{-1}) peak, which is associated with the structural defects of carbon, and G (1580 cm^{-1}) peak, which is associated with in-plane vibration of sp^2 hybridized carbon atoms, further confirm that the carbon material present in the electrode is graphitic oxide in nature.[32] The well-defined Raman spectrum signifies the good crystallinity of the as-prepared MnO_x-rGO electrode.

3.4. Electrochemical properties

To investigate the electrochemical performance of the as-prepared MnO_x-rGO electrode, electrochemical measurements, such as CV, GCD and EIS, were carried out in 1 M KOH. CV measurements were carried out in the potential range between 0.0 to 0.6 V at various scan rates ranging from 10 to 100 mV s^{-1}. Fig. 5 (a) compares the CV curves at 50 mV s^{-1} scan rate for the Pt–Si substrate and the as-synthesized MnO_x-rGO electrode. It can be clearly seen from the figure that the substrate has no contribution to the electrochemical performance of the electrode. Fig. 5(b) shows the CV curves for MnO_x-rGO electrode at various scan rates.

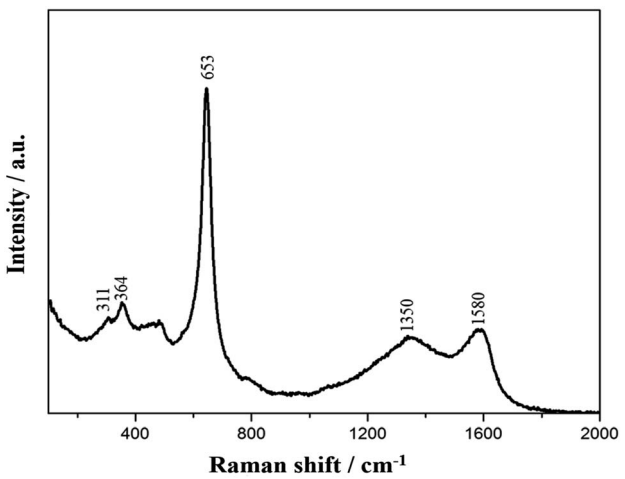

Fig. 4 Raman spectrum of MnO_x-rGO electrode.

The presence of the well-defined redox peaks in the CV curves at all scan rates indicates that the electrochemical capacitance of the electrode results from the pseudocapacitive charge storage mechanism. As obtained CV curves are similar to those previously reported[42,43] with a slight difference in the redox peak potentials, which could be attributed to the unique morphology and nanostructure of the electrode. The increase in the area of the CV curves with increasing scan rates suggests the higher charge storage capability and good reversibility of the electrode along with fast electrons and ion diffusion rate in the electrode. Anodic peak around 0.45 V and cathodic peak around 0.40 V mainly come from the reversible faradaic redox reactions of active material and the electrolyte. With the increase in scan rate, anodic peak current has increased, and cathodic peak current has decreased, suggesting relatively low resistance of the electrode and fast redox reaction at the interface of the electrode and the electrolyte.[44] Additionally, the anodic and cathodic peaks show slight positive and negative shifts, respectively, with increasing scan rates, due to the internal resistance of the electrode.

The capacitance of the electrode mainly depends on the two possible charge storage mechanisms in the electrode. The first one is the intercalation of alkali metal cations (C^+), such as K^+, during reduction and de-intercalation during the oxidation in the electrode;[45]

$$MnO_2 + C^+ + e^- \leftrightarrow MnOOC^+ \quad (1)$$

The second one is that the cations in the electrolyte are adsorbed at the manganese oxide electrode:

$$(MnO_2)_{surface} + C^+ + e^- \leftrightarrow (MnO_2{-}C^+)_{surface} \quad (2)$$

Also, possible pseudo-capacitive mechanism for Mn_3O_4 electrode in KOH electrolyte can be given by following relations;[46]

$$3Mn(OH)_2 + 2OH^- \leftrightarrow Mn_3O_4{\cdot}2H_2O + 2e^- + 2H_2O \quad (3)$$

$$Mn_3O_4{\cdot}2H_2O + OH^- \leftrightarrow 2MnOOH + Mn(OH)_3 + e^- \quad (4)$$

Rapid transfer of K^+ cation and electrons help accelerate the above charge storage reactions. Because of the high porosity, a greater surface area of the electrode is accessible for the electrolyte. Moreover, the porous structure shortens the ion diffusion length that helps facilitate the transfer of electron and ions involved in the redox reactions.[47,48] Also, the minimal change in the shape of the CV curves, which can be attributed to the porous nanostructure that allows for greater interaction between the active material and the electrolyte, at higher scan rates suggests a small equivalent series resistance (ESR),[49]

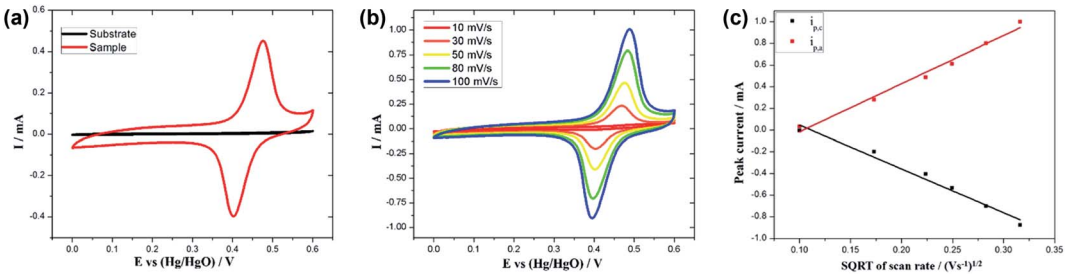

Fig. 5 (a) CV curves at 50 mV s^{-1} scan rate for the Pt–Si substrate and the MnO_x-rGO electrode, (b) CV curves at various scan rates for MnO_x-rGO electrode, and (c) Randles–Sevcik plot for the MnO_x-rGO electrode, where $i_{p,c}$ and $i_{p,a}$ refer to cathodic and anodic peak currents, respectively.

excellent rate performance and electrochemical reversibility of the electrode.

Fig. 5(c) shows a plot of anodic and cathodic peak currents *vs.* square root of scan rates, known as the Randles–Sevcik plot, for the as-prepared MnO_x-rGO electrode. For both the anodic and cathodic peak current densities, straight lines can be seen in the figure, which suggests the diffusion-controlled rate kinetics is the dominating mechanism of the redox processes.[13,50]

In order to further evaluate the electrochemical performance of the electrode, GCD measurements were performed in the potential range from 0.0 to 0.6 V (*vs.* Hg/HgO). Fig. 6(a) shows the schematic of a typical GCD curve for pseudocapacitors, with a characteristic internal resistance (IR) drop at the start of the discharge process. We performed charge–discharge measurements at various current densities for the MnO_x-rGO electrode, as shown in Fig. 6(b). It can be seen that all the curves are nonlinear, which further indicates the pseudocapacitive behavior of the electrode, and contain a very small IR drop, indicating the low ESR of the electrode.

It is well known that calculating capacitance from a discharge curve is the most commonly used method. Therefore, the areal specific capacitance at various current densities of the electrode was calculated from the GCD curves by using the following equation;[51]

$$C = \frac{I\Delta t}{A\Delta V} \quad (5)$$

where I is the discharge current (mA), Δt is the discharge time (s), A is the area of the electrode (cm^2) and ΔV is the potential (V) change during discharge excluding the IR drop.

Initially, the specific capacitance is calculated to be 11 mF cm^{-2} and as the number of cycles increased, a slight decrease in the capacitance is recorded.

Cycling stability is another important requirement for supercapacitor electrodes. To test the cycling stability of the MnO_x-rGO electrode, the GCD measurements were carried out for 100,000 continuous cycles at constant areal current density of 0.4 mA cm^{-2}. Fig. 7(a) shows the trend of areal specific capacitance *versus* the number of GCD cycles at constant areal current density of 0.4 mA cm^{-2}. Finally, even after 100 000 GCD cycles, the capacitance is calculated to be 10 mF cm^{-2}. This shows the excellent life cycle and the electrochemical stability of the MnO_x-rGO electrode. The percentage of specific capacitance retention is calculated after a various number of cycles and are plotted in Fig. 7(b). It can be seen that the MnO_x-rGO electrode has excellent capacitance retention as it retains 90% of initial capacitance even after 100 000 GCD cycles, exhibiting excellent electrochemical and cycling stability as well as ultra-long cycle life. Such excellent electrochemical performance of the electrode can be attributed to the pseudocapacitive behavior of the electrode as well as the highly porous 3D morphology that

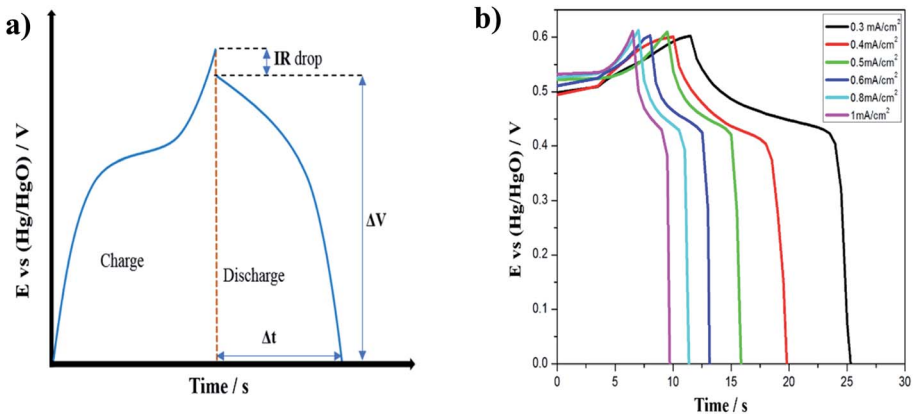

Fig. 6 (a) Schematic of a GCD curve for a pseudocapacitor and (b) GCD curves for MnO_x-rGO electrode at various areal current densities.

allows for easy intercalation and de-intercalation of high-mobility K^+ ions. Additionally, such porous morphology contributes to the electrochemical performance of the electrode by providing a buffer during volume changes. The number of GCD cycles we performed is significantly greater than what is reported in the literature for most of the manganese-oxide based supercapacitor electrodes.[10,43,45,50,52–54] The excellent performance of the as-prepared electrode in terms of long-term cycling stability is superior to the metal-oxide based supercapacitor electrodes previously reported. The slight decrease in capacitance after 100 000 GCD cycles can be attributed to irreversible faradaic redox reactions or the physical change in nanostructures in the process of OH^- insertion/extraction during oxidation/reduction. These excellent electrochemical performances demonstrate the MnO_x-rGO electrode's potential for application in long-term electronics.

Another important parameter of the electrochemical measurement is the rate capability measurement, which is related to the rate of ion diffusion in the electrode.[33] To test the rate capability of the electrode, GCD measurements were performed at various current densities and specific capacitance at various current densities was calculated, which is shown in Fig. 7(c). We can see from the figure that even at 1.5 mA cm^{-2} current density, the electrode maintains a specific capacitance of 8.5 mF cm^{-2}, exhibiting a good rate capability. At lower current densities, electrolyte ions get enough time to fully access the bulk of active material and an increased rate of intercalation/deintercalation takes place, which results in higher capacitance. On the other hand, at high current densities, the ions suffer from a low diffusion and cannot penetrate deep into the active material and only the outer surface of the electrode could take part in the redox reactions, thereby decreasing the effective interaction between the active material and the electrolyte. This is why the electrode shows low capacitance at higher current densities.

The coulombic efficiency of the electrode was also evaluated from the GCD curves by using the following equation;[55]

$$\eta = \frac{Q_d}{Q_c} \times 100\% = \frac{\Delta t_d}{\Delta t_c} \times 100\% \quad (6)$$

where Q_d and Q_c are charges for discharge and charge processes, respectively, and Δt_c and Δt_d are the charging and discharging time, respectively. From Fig. 7(b) we can see that after 100 000 GCD cycles, the electrode maintains a coulombic efficiency of 95%, indicating the excellent performance of the electrode.

To further understand the electrochemical behavior of the MnO_x-rGO electrode, EIS was performed. This is an effective method to study the fundamental behavior of electrode materials and the relationship between capacitive properties and electronic as well as ionic resistance of the electrode.[56] An EIS plot is presented in the form of a Nyquist plot, where imaginary

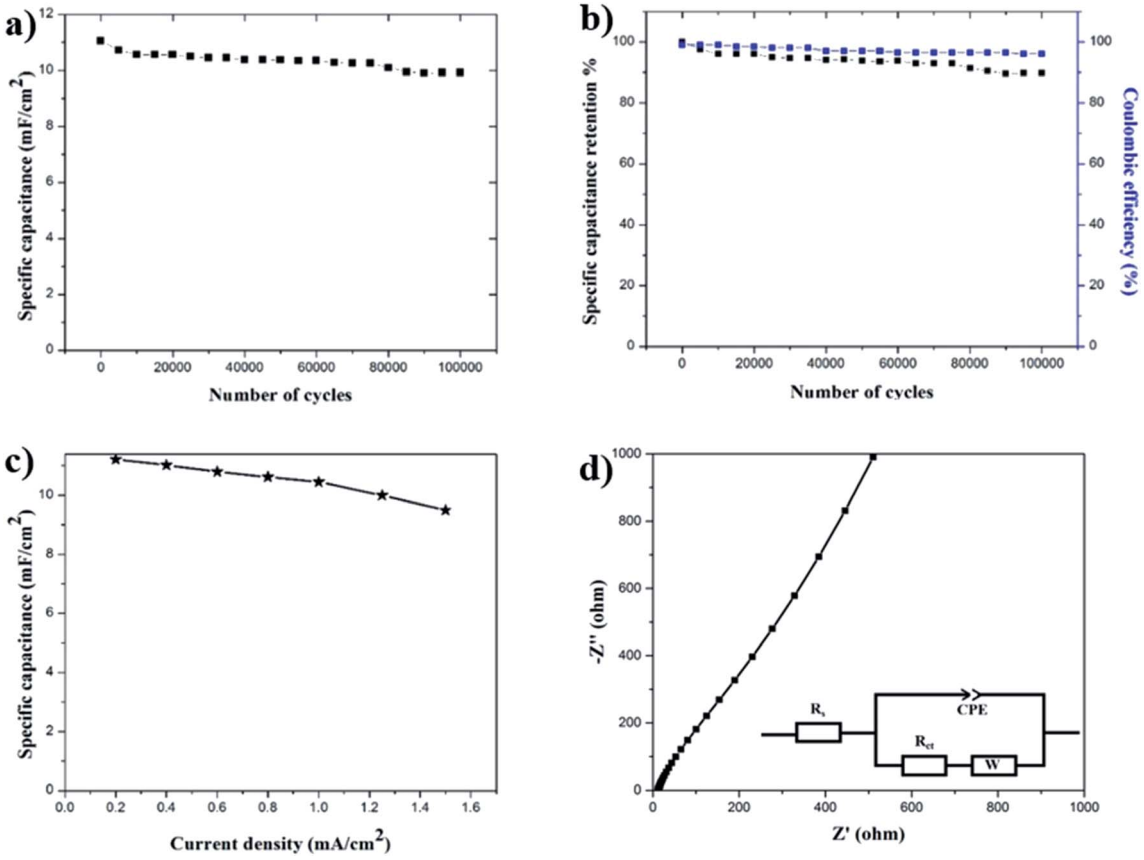

Fig. 7 (a) Specific capacitance at 0.4 mA cm^{-2} constant areal current density, (b) capacitance retention and coulombic efficiency, (c) specific capacitance at various current densities, and (d) Nyquist plot for EIS measurements with equivalent circuit for MnO_x-rGO electrode.

and real impedance are plotted against each other over a wide frequency range. A typical Nyquist plot contains a semicircle at higher frequencies that corresponds to the limited charge-transfer process, and a linear region at lower frequencies due to Warburg resistance (W), which is a result of the frequency dependence of ionic diffusion/transport in the electrolyte and to the surface of the electrode.[57–59] For ideal capacitive behavior, the plot in low frequency region is supposed to be parallel to the imaginary *Z*-axis. Moreover, the intercept in the *x*-axis of a Nyquist plot gives the total internal resistance (R_s) that is the combination of the ionic resistance of the electrolyte, intrinsic resistance of the substrate and contact resistance between the active material and the current collector.[60] The diameter of the semicircle at the high frequency region gives the charge transfer resistance (R_{ct}), resulting from the faradaic reactions and the double-layer capacitance (C_{dl}) on the electrode surface.[53] For the as-prepared MnO_x-rGO electrode, we performed EIS measurements at room temperature over a frequency range of 1 MHz to 10 mHz, as shown in Fig. 7(d). From this measurement, the series resistance of the MnO_x-rGO electrode is calculated to be 12.85 Ω. This could be because of the relatively poor conductivity of the electrode. Additionally, as can be seen from the figure, the EIS plot does not contain a semicircle at high frequency region, which is indicative of a very low charge transfer resistance of the electrode.[61] This could also be another factor contributing to excellent electrochemical performance of the electrode.

4. Conclusions

In summary, we presented an extremely convenient and cost-effective one-step method to synthesize highly porous 3D nanostructured manganese oxide-reduced graphitic oxide (MnO_x-rGO) thin film electrode. By following the photonic curing technique, we have significantly reduced the typically hours long processing time (in case of conventional techniques) to several seconds. To our knowledge, such a quick processing technique has not been reported for the fabrication of metal oxide supercapacitor electrodes. The specific capacitance of the as-prepared MnO_x-rGO oxide electrode was 11 mF cm^{-2} at a constant current density of 0.4 mA cm^{-2}. Even after 100 000 GCD cycles, the electrode retained 90% of its initial capacitance, exhibiting excellent electrochemical stability and ultra-long lifetime. These excellent results can be attributed to the increased conductivity resulting from the conductive rGO component, the synergistic effect of carbon composite and the metal oxide, optimum processing conditions and a highly porous nanostructure, which offers enhanced ions/electron movement and high electrolyte-accessible surface area. The capacitance calculated at various current densities shows that the electrode exhibits high rate capability. In consideration of the excellent electrochemical performance, simple and quick preparation method, and very short processing time (several seconds), as prepared manganese oxide-reduced graphitic oxide (MnO_x-rGO) electrode shows promising potential for application as supercapacitor electrodes. More importantly, the ultra-long lifetime of the electrode signifies its potential in long-term electronics applications.

Conflicts of interest

There are no conflicts to declare.

Acknowledgements

This work was financially supported by Louisiana Board of Regents, Industrial Ties to Research Subprogram, Grant Number LEQSF (2017-20)-RD-B-04.

References

1 Z. Gao, W. Yang, J. Wang, N. Song and X. Li, *Nano Energy*, 2015, **13**, 306–317.
2 K. Liang, T. Gu, Z. Cao, X. Tang, W. Hu and B. Wei, *Nano Energy*, 2014, **9**, 245–251.
3 Y. Wu, S. Liu, H. Wang, X. Wang, X. Zhang and G. Jin, *Electrochim. Acta*, 2013, **90**, 210–218.
4 C. H. Ng, H. N. Lim, S. Hayase, Z. Zainal, S. Shafie and N. M. Huang, *Ind. Eng. Chem. Res.*, 2018, **57**, 2146–2154.
5 K. Liang, X. Tang, B. Wei and W. Hu, *Mater. Res. Bull.*, 2013, **48**, 3829–3833.
6 E. Mitchell, R. K. Gupta, K. Mensah-Darkwa, D. Kumar, K. Ramasamy, B. K. Gupta and P. Kahol, *New J. Chem.*, 2014, **38**, 4344–4350.
7 K. Liang, K. Marcus, Z. Yang, L. Zhou, H. Pan, Y. Bai, Y. Du, M. H. Engelhard and Y. Yang, *Small*, 2018, **14**, 1702295.
8 B. Pandit, D. P. Dubal and B. R. Sankapal, *Electrochim. Acta*, 2017, **242**, 382–389.
9 P. Yang and W. Mai, *Nano Energy*, 2014, **8**, 274–290.
10 M. S. Wu and H. H. Hsieh, *Electrochim. Acta*, 2008, **53**, 3427–3435.
11 Z. S. Wu, W. Ren, D. W. Wang, F. Li, B. Liu and H. M. Cheng, *ACS Nano*, 2010, **4**, 5835–5842.
12 Y. T. Wang, A. H. Lu, H. L. Zhang and W. C. Li, *J. Phys. Chem. C*, 2011, **115**, 5413–5421.
13 R. Manikandan, C. J. Raj, M. Rajesh, B. C. Kim, J. Y. Sim and K. H. Yu, *ChemElectroChem*, 2018, 101.
14 X. Lin, H. Lou, W. Lu, F. Xu, R. Fu and D. Wu, *Chin. Chem. Lett.*, 2018, **29**, 633–636.
15 H. Wu, X. Wang, L. Jiang, C. Wu, Q. Zhao, X. Liu, B. Hu and L. Yi, *J. Power Sources*, 2013, **226**, 202–209.
16 C. J. Raj, M. Rajesh, R. Manikandan, J. Y. Sim, K. H. Yu, S. Y. Park, J. H. Song and B. C. Kim, *Electrochim. Acta*, 2017, **247**, 949–957.
17 S. Ortaboy, J. P. Alper, F. Rossi, G. Bertoni, G. Salviati, C. Carraro and R. Maboudian, *Energy Environ. Sci.*, 2017, **10**, 1505–1516.
18 M. Sawangphruk, P. Srimuk, P. Chiochan, A. Krittayavathananon, S. Luanwuthi and J. Limtrakul, *Carbon*, 2013, **60**, 109–116.
19 B. Wang, J. Park, C. Wang, H. Ahn and G. Wang, *Electrochim. Acta*, 2010, **55**, 6812–6817.

20 R. Amade, E. Jover, B. Caglar, T. Mutlu and E. Bertran, *J. Power Sources*, 2011, **196**, 5779–5783.
21 H. Jiang, J. Ma and C. Li, *Adv. Mater.*, 2012, **24**, 4197–4202.
22 R. B. Rakhi, W. Chen, D. Cha and H. N. Alshareef, *J. Mater. Chem.*, 2011, **21**, 16197–16204.
23 Y. Hou, Y. Cheng, T. Hobson and J. Liu, *Nano Lett.*, 2010, **10**, 2727–2733.
24 J. M. Ko and K. M. Kim, *Mater. Chem. Phys.*, 2009, **114**, 837–841.
25 R. K. Sharma, H. S. Oh, Y. G. Shul and H. Kim, *J. Power Sources*, 2007, **173**, 1024–1028.
26 W. Meng, W. Chen, L. Zhao, Y. Huang, M. Zhu, Y. Huang, Y. Fu, F. Geng, J. Yu, X. Chen and C. Zhi, *Nano Energy*, 2014, **8**, 133–140.
27 G. Lota, K. Fic and E. Frackowiak, *Energy Environ. Sci.*, 2011, **4**, 1592–1605.
28 Z. Li, Y. Mi, X. Liu, S. Liu, S. Yang and J. Wang, *J. Mater. Chem.*, 2011, **21**, 14706–14711.
29 S. Bose, T. Kuila, A. K. Mishra, R. Rajasekar, N. H. Kim and J. H. Lee, *J. Mater. Chem.*, 2012, **22**, 767–784.
30 S. Luo, S. Zhang, B. B. Bourgeois, B. C. Riggs, K. A. Schroder, Y. Zhang, J. He, S. Adireddy, K. Sun, J. T. Shipman, M. M. Oguntoye, V. Puli, W. Liu, R. Tu, L. Zhang, S. Farnsworth and D. B. Chrisey, *J. Mater. Res.*, 2017, **32**, 1701–1709.
31 B. Bourgeois, S. Luo, B. Riggs, Y. Ji, S. Adireddy, K. Schroder, S. Farnsworth, D. Chrisey and M. Escarra, *Nanotechnology*, 2018, **29**, 315401.
32 B. B. Bourgeois, S. Luo, B. C. Riggs, S. Adireddy and D. B. Chrisey, *Appl. Phys. A: Mater. Sci. Process.*, 2017, **123**, 588.
33 Y. Wang, W. Chen, B. Wang and Y. Zheng, *Materials*, 2014, **7**, 6377–6485.
34 A. A. Virkar, S. Mannsfeld, Z. Bao and N. Stingelin, *Adv. Mater.*, 2010, **22**, 3857–3875.
35 X. Yang, P. Gao, Z. Yang, J. Zhu, F. Huang and J. Ye, *Sci. Rep.*, 2017, **7**, 1–9.
36 K. Tetzner, Y. H. Lin, A. Regoutz, A. Seitkhan, D. J. Payne and T. D. Anthopoulos, *J. Mater. Chem. C*, 2017, **5**, 11724–11732.
37 P. Iamprasertkun, A. Krittayavathananon, A. Seubsai, N. Chanlek, P. Kidkhunthod, W. Sangthong, S. Maensiri, R. Yimnirun, S. Nilmoung, P. Pannopard, S. Ittisanronnachai, K. Kongpatpanich, J. Limtrakul and M. Sawangphruk, *Sci. Rep.*, 2016, **6**, 1–12.
38 I. Stoševski, A. Bonakdarpour, F. Cuadra and D. P. Wilkinson, *Chem. Commun.*, 2019, **55**, 2082–2085.
39 S. Hirai, A. M. Dos Santos, M. C. Shapiro, J. J. Molaison, N. Pradhan, M. Guthrie, C. A. Tulk, I. R. Fisher and W. L. Mao, *Phys. Rev. B: Condens. Matter Mater. Phys.*, 2013, **87**, 014417.
40 F. Xiao and Y. Xu, *Int. J. Electrochem. Sci.*, 2012, **7**, 7440–7450.
41 C. M. Julien, M. Massot and C. Poinsignon, *Spectrochim. Acta, Part A*, 2004, **60**, 689–700.
42 H. U. Shah, F. Wang, A. M. Toufiq, A. M. Khattak, A. Iqbal, Z. A. Ghazi, S. Ali, X. Li and Z. Wang, *Int. J. Electrochem. Sci.*, 2016, **11**, 8155–8162.
43 J. Shin, D. Shin, H. Hwang, T. Yeo, S. Park and W. Choi, *J. Mater. Chem. A*, 2017, **5**, 13488–13498.
44 W. Li, B. Zhang, R. Lin, S. M. Ho-Kimura, G. He, X. Zhou, J. Hu and I. P. Parkin, *Adv. Funct. Mater.*, 2018, **28**, 1705937.
45 M. Feng, Q. Du, L. Su, G. Zhang, G. Wang, Z. Ma, W. Gao, X. Qin and G. Shao, *Sci. Rep.*, 2017, **7**, 1–8.
46 L. He, G. Zhang, Y. Dong, Z. Zhang, S. Xue and X. Jiang, *Nano-Micro Lett.*, 2014, **6**, 38–45.
47 M. Zhi, C. Xiang, J. Li, M. Li and N. Wu, *Nanoscale*, 2013, **5**, 72–88.
48 R. Wang and X. Yan, *Sci. Rep.*, 2014, **4**, 3712.
49 T. Zhai, F. Wang, M. Yu, S. Xie, C. Liang, C. Li, F. Xiao, R. Tang, Q. Wu, X. Lu and Y. Tong, *Nanoscale*, 2013, **5**, 6790–6796.
50 A. N. Naveen and S. Selladurai, *RSC Adv.*, 2015, **5**, 65139–65152.
51 H. An, Y. Wang, X. Wang, N. Li and L. Zheng, *J. Solid State Electrochem.*, 2010, **14**, 651–657.
52 X. Lu, D. Zheng, T. Zhai, Z. Liu, Y. Huang, S. Xie and Y. Tong, *Energy Environ. Sci.*, 2011, **4**, 2915–2921.
53 W. Yang, Z. Gao, J. Wang, B. Wang, Q. Liu, Z. Li, T. Mann, P. Yang, M. Zhang and L. Liu, *Electrochim. Acta*, 2012, **69**, 112–119.
54 Q. Cheng, J. Tang, J. Ma, H. Zhang, N. Shinya and L. C. Qin, *Carbon*, 2011, **49**, 2917–2925.
55 A. Mirmohseni, M. S. S. Dorraji and M. G. Hosseini, *Electrochim. Acta*, 2012, **70**, 182–192.
56 S. Afriyanti, F. C. Yao, W. Xu and L. P. See, *Adv. Mater.*, 2013, **25**, 2809–2815.
57 E. Lohrasbi and M. Asgari, *Adv. Anal. Chem.*, 2015, **5**, 9–18.
58 S. Dhibar, P. Bhattacharya, G. Hatui and C. K. Das, *J. Alloys Compd.*, 2015, **625**, 64–75.
59 J. Yan, J. Liu, Z. Fan, T. Wei and L. Zhang, *Carbon*, 2012, **50**, 2179–2188.
60 L. Wang, H. Ji, S. Wang, L. Kong, X. Jiang and G. Yang, *Nanoscale*, 2013, **5**, 3793–3799.
61 N. Bundaleska, J. Henriques, M. Abrashev, A. M. Botelho do Rego, A. M. Ferraria, A. Almeida, F. M. Dias, E. Valcheva, B. Arnaudov, K. K. Upadhyay, M. F. Montemor and E. Tatarova, *Sci. Rep.*, 2018, **8**, 12595.